A MEMS Mirror-Based Confocal Laser Endomicroscope with Image Distortion Correction

Teng Pan ©, Xun Gao ©, Hengzhang Yang ©, Yingchao Cao, Hui Zhao, Qian Chen, and Huikai Xie ©, *Fellow, IEEE*

Abstract—Scanning MEMS mirrors can extend confocal laser microscopy into endoscopic applications, but the practical use of MEMS mirror-based confocal endomicroscopy is hindered partially by various image distortions such as barrel, fan-shaped and nonlinear distortions. In this work, the nonlinear scanning behaviors of an electrothermal MEMS mirror are analyzed and incorporated into an optical scanning model that takes all these three types of distortions into account. The model generates a 2D spatial mapping that can be applied to correct all of the image distortions in one step without a calibration board. To experimentally validate this method, a confocal laser endomicroscope employing a two-axis scanning electrothermal MEMS micromirror is designed and constructed, and confocal fluorescence images of a patterned micro-structure are obtained with the endomicroscope. The results show that the overall image distortion is reduced by at least one order of magnitude in the length direction.

Index Terms—Confocal imaging, endomicroscope, MEMS mirror, distortion correction, nonlinear.

I. INTRODUCTION

CONFOCAL microscopy is an important optical biomedical imaging technology and possesses diffraction-limited resolution, optical sectioning ability and simple configuration [1]. Compared to ultrasound (US), magnetic resonance imaging (MRI), and computed tomography (CT), confocal imaging has much higher resolution and lower risk, but it has shallow penetration depth [2]. Thus, endoscopic confocal microscopy is needed to access internal organs. Combined diagnosis of morphology and histology has been reported by integrating confocal imaging into endoscopes [3], [4].

Confocal laser endomicroscope (CLE) is basically divided into distal and proximal scanning types based on the position of the laser scanning mechanism [5], [6]. Proximal scanning is typically performed by utilizing galvanometers scanning the

laser on the proximal end of a fiber bundle that relays the scanned laser pattern to the tissue of interest inside an internal organ. This method avoids the need to miniaturize the scanning devices, but the achievable resolution and field of view (FOV) are limited by the spacing of the individual fibers and the numbers of fibers within the bundle [7], [8]. To achieve optical diffraction-limited resolution, endoscope-based CLEs use single or two optical fibers to guide a laser beam steered across the tissue by small-sized laser scanners that are integrated into the distal tip of an endoscopic probe, called distal scanning [9].

A variety of scanning mechanisms have been employed in distal scanning CLEs, including piezoelectric fiber scanners [10], electromagnetically actuated resonant armature systems [7], and various microelectromechanical system (MEMS) mirrors [11], [12], but scanning MEMS mirrors are drawing the most attention. In past decades, electrostatic [13], [14], [15], [16], piezoelectric [17], [18], electromagnetic [19], and electrothermal [20], [21] MEMS mirrors have been applied to miniaturize confocal microscopes. However, image distortions are always generated due to the non-ideal movement characteristics of MEMS mirrors, such as nonlinear motion and temperature drift. The MEMS mirrors actuated at resonant states exhibit a sinusoidal motion, causing nonuniform scan in time domain [22], which can be corrected by a re-indexing of the rendered image [23]. A computer vision-based image de-warping method can be used to correct the non-uniform distortion in optical coherence tomography (OCT) images with test checkerboard patterns [24]. Hardware methods have also been reported for distortion-free imaging without post-processing in OCT systems. For example, the linear motion of scanning MEMS mirrors may be obtained using an open-loop pre-shaped input signal [25], [26]. However, unlike endoscopic OCT, a distal scanning CLE further suffers from the radial distortion due to the high numerical aperture (NA) of the small-sized objective lens. In addition, imaging quality is also affected by the optical layout in a MEMS-based laser scanning system. For example, fan-shaped distortion is resultant when the incident laser light is reflected by a tip-tilt micromirror [27]. A number of correction methods have been developed to deal with fan-shaped distortions, such as numerical modelling [28], grating target calibration [29] and simplified first-order analytical modelling [30]. Co-contribution of multiple distortions degrades imaging quality of CLEs, causing low diagnostic accuracy. A standard calibration board may be used to correct multiple distortions, but this method only works for a reflectance CLE because the thickness of a standard board (typically 1–1.5 mm) may be even greater than the working
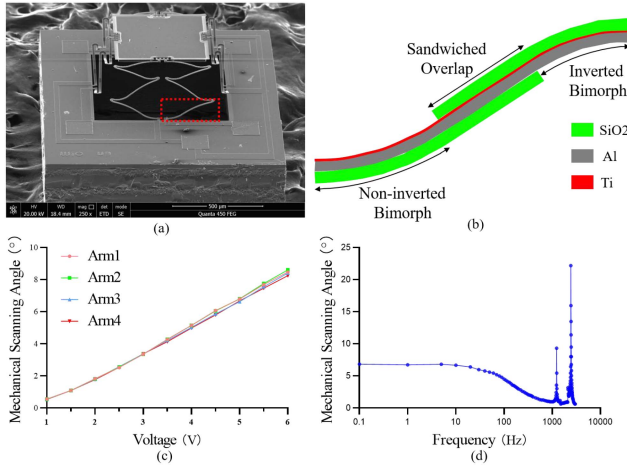
Fig. 1. A MEMS mirror employed in a CLE. (a) An SEM image. (b) An illustration of one S-shaped ISC bimorph beam marked the red box of (a). (c) Quasi-static response. (d) Frequency response.
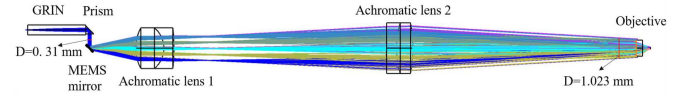

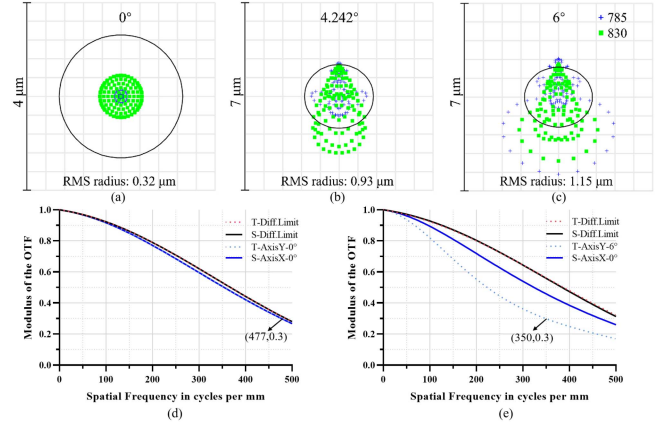Fig. 2. The optical layout of the confocal endoscopic probe.

Fig. 3. Simulation performance of the optical design. (a)–(c) Geometric spot diagrams at 785 nm and 830 nm for three MEMS scanning angles: 0°, 4.242°, 6°. (d)–(e) Modulation transfer function plots calculated at all wavelengths (785 nm and 830 nm) for axis (d) and marginal (e) points, respectively.

distance (<1 mm) of a fluorescence CLE [5]. Fluorescence confocal microscopy is much more widely used in clinical practice because of its high specificity provided by various fluorophores. Therefore, a method without calibration boards is needed for a clinically useful confocal endomicroscope to correct simultaneously all of the distortions caused by the optical layout, high-NA objective lens, and MEMS nonlinear motion.

In this work, a new model-based image correction method is proposed to correct the optical and nonlinear distortions of a MEMS-based confocal endomicroscope in one step. A CLE probe based on a two-axis scanning electrothermal MEMS mirror is built to verify the proposed method. This CLE probe is smaller and more robust compared to previous work using similar electrothermal actuators [21], [31]. This paper is arranged as follows. The MEMS mirror employed, the optical design and integration of the CLE system are described in Section II. The optical and nonlinear distortions are analyzed and then the proposed correction method is presented in Section III. After that, the experimental verification results are given and discussed in Section IV.

II. THE MEMS-BASED CONFOCAL LASER ENDOMICROSCOPE

A. The Two-Axis Electrothermally Actuated MEMS Mirror

The 2-axis MEMS mirror is the key component of the endoscopic probe that enables raster scanning in a narrow-confined channel. A scanning electron microscope (SEM) image of the mirror is shown in Fig. 1(a). The MEMS mirror has a footprint of 1.5 mm × 1.3 mm and a square mirror plate with a side length of 550 μm. The mirror plate is supported by four symmetrically-placed S-shaped bimorph structures. One S-shaped bimorph arm with an inverted-series-connected (ISC) structure is illustrated in Fig. 1(b), consisting of a non-inverted bimorph, a sandwiched overlap segment, and an inverted bimorph. Each bimorph deforms upon temperature change due to the difference of the thermal expansion coefficients between aluminum (Al) and silicon dioxide (SiO2). The deformations of the bimorphs

change the orientation and/or elevation of the mirror plate. The temperature change is generated by a resistive heater made of titanium (Ti) stripe embedded in the bimorph beams. When driving voltages are applied to the four bimorph actuators, the mirror plate performs tip-tilt-piston movement. The measured quasi-static and frequency response of the employed MEMS mirror are shown in Fig. 1(c) and (d), respectively.

B. Optical Design of the Confocal Endoscopic Probe

The optical layout of the proposed probe is shown in Fig. 2, where a MEMS mirror chip is placed on an inclined plane of 45° with respect to the optical axis. A graded-index (GRIN) lens and a prism are used to collimate and reflect a laser beam (diameter: 0.31 mm) onto the MEMS mirror. Two achromatic lenses (Edmund, 63714 & 49302) form a 4-f imaging system, resulting in a 3.3× magnified laser beam (diameter: 1.023 mm) to perform telecentric scanning on the back focal plane of the objective lens (Thorlabs, 354140-B).

The above optical system has been simulated using the Zemax Optic Studio software [32]. The spot diagrams at different MEMS scanning angles are shown in Fig. 3(a)–(c). It is obvious that the larger the scanning angle is, the greater the spot size becomes. As shown in Fig. 3(c), the RMS spot radius at 6° scanning angle (y-axis) is 1.15 μm, which is less than the Airy radii, i.e., 1.18 μm and 1.25 μm, of both the excitation light (785 nm) and the emission light (830 nm peak wavelength). The modulation transfer functions (MTFs) are calculated under two wavelength condition, and the MTFs are classified as the sagittal and tangential correction at a diffraction limit, 0° and 6° field angle. The MTFs at 0° and 6° are plotted in Fig. 3(d)
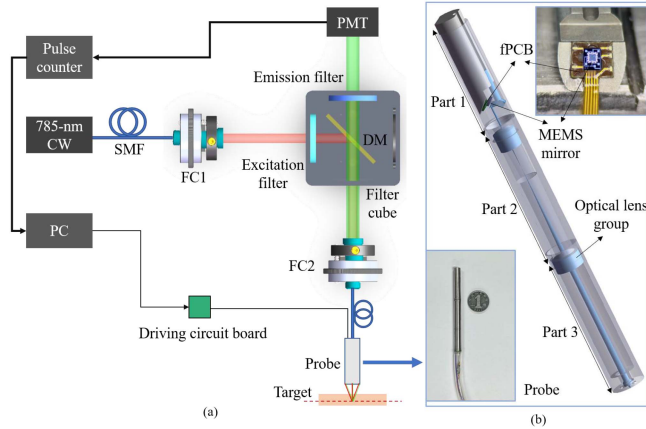
Fig. 4. The system setup. (a) The illustration of the CLE system. (b) The mechanical design of the probe assembly. The inset (lower left) is a photograph of the assembled probe beside a Chinese Yuan coin. The packaged MEMS mirror is shown in the upper right inset.

and (e), respectively, where the best and worst lateral resolvable distance at 0.3 modulus are 1.05 μm and 1.42 μm on the optical axis and at the edge of the field of view, respectively. Thus, this design meets the diffraction limited resolution both at axial and marginal lines. The theoretical axial resolution of the confocal probe is 10.10 μm [33].

C. System Integration

The schematic diagram of the MEMS-based CLE system is shown in Fig. 4(a), where a CW laser diode (Boson, FC-785-070-SM-APC) is used as the excitation light source (center wavelength: 785 nm). The laser beam emitting from a single mode fiber (SMF) is coupled into a fiber collimator (FC1) (Thorlabs, F280APC-780). The laser beam is filtered through an excitation filter (Semrock, FF01-769/41-25) and then reflected by a dichroic mirror (DM) (Semrock, FF801-Di02-25x36) into another fiber collimator (FC2). Two collimators are mounted in two collimator adapters (Thorlabs, KAD11F) to improve optical coupling efficiency. The focused laser beam is coupled into a home-made confocal endoscopic probe with a SMF (Nufern, 780-HP) pigtail. The laser emitting from the probe is shined on a target and a raster scanning pattern is generated by the MEMS mirror driven by a custom circuit board. The object is pre-injected with indocyanine green (ICG) fluorophores, so fluorescence is generated. The emitted light is collected by the objective lens and de-scanned into the SMF whose core is used as the confocal pinhole to remove out-of-focus light. An emission filter (Semrock, FF01-832/37) mounted in a filter cube is used to separate the excitation and emission light. The fluorescence is collected by a photomultiplier (PMT) module (Hamamatsu, H8259-02) after passing through the emission filter. The PMT module converts the fluorescent photons to pulse signals that are then transmitted to an electronic pulse counter implemented on an FPGA kit (TERASIC, C5G). The pulse counter is connected to a personal computer (PC) via a USB cable. Additionally, LabVIEW software is used for image collection, storage and display.
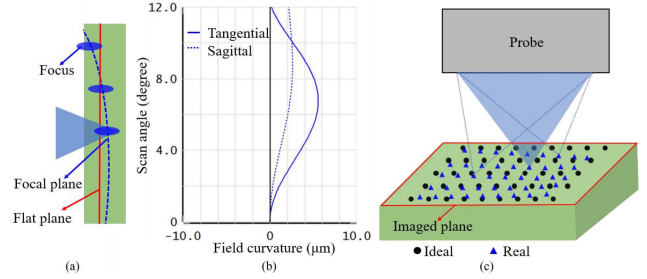

Fig. 5. Illustration of the 2-D scanning pattern in confocal imaging. (a) The difference between the focal plane and the flat plane. (b) Field curvature. (c) The ideal and real raster scanning patterns.

The mechnical structure of the MEMS-based probe is shown in Fig. 4(b), where the MEMS mirror is integrated into the distal end of the probe that consists of a stainless-steel housing and optical components. Part 1 of the housing consists of a GRIN lens, a prism, a MEMS mirror, and a flexible PCB. The MEMS mirror is wire-bonded to the flexible PCB using gold bond wires as shown in the upper right inset. Two achromatic lenses and an objective lens are fixed into Part 2 and Part 3 with UV glue. The lower left inset in Fig. 4(b) shows the assembled probe whose length and diameter are 72 mm and 6 mm, respectively.

III. DISTORTION ANALYSIS AND CORRECTION METHOD

The confocal imaging is a point-by-point scanning process using a pinhole to obtain optical signals in focal spots. For rotational scanning, the focal plane is curved, as shown in Fig. 5(a). The maximum deviations from a perfect plane to both of the tangential and sagittal directions are less than 6 μm in the optical scan angles ranging from 0° to 12°, as shown in Fig. 5(b). As discussed in II.B, the axial resolution of this confocal system is about 10 μm. Therefore, the focal plane can be treated as a flat plane. During the confocal imaging, fluorescent light signals are acquired at different focal planes. The 2D raster scanning pattern at one focal plane is illustrated in Fig. 5(c), where the actual MEMS scanned points on the focal plane are marked as blue triangles while the ideal scanning pattern with a uniform linear distribution is represented with black points. Due to the nonlinear raster scanning behavior of the MEMS mirror, the real scanning pattern (RSP) shown in blue triangles is distorted. If the distorted RSP is not considered in the image reconstruction process, the reconstructed image will be distorted as well.

A. Distortion Analysis

As shown in Fig. 6(a), an optical scanning model is built in Zemax to analyze distortions generated by the optical factors, i.e., optical layout and miniature high-NA lens, which will cause fan-shaped distortions and barrel distortions, respectively. The MEMS mirror plate X'O'Y' in its still state is angled at $\beta = 45°$ to both the incident and reflected laser beams as shown in Fig. 6(b). When the two-axis mirror is deflected from −6° to 6° in a linear raster manner, the reflected beams will be projected into a fan-shaped pattern (blue dots) in the plane XOY, as shown in
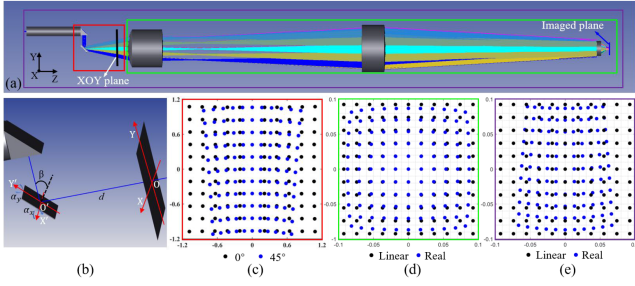
Fig. 6. The distortions caused by the optical factors. (a) The optical scanning model. (b) The optical layout with the MEMS oriented at 45°. (c) The fan-shaped distortion caused by the optical layout in (b). (d) The barrel distortion resulted from the lens group. (e) The optical distortions caused by both the optical layout and the lens group.

Fig. 6(c), so called fan-shaped distortion. Note that the perfect projection pattern (black dots) at $\beta = 0°$ is also plotted in Fig. 6(c) as a reference. The positions of the blue dots can be obtained using the following equations [27],

$$
\begin{cases}
X = d\dfrac{\cos(\beta-\alpha_x)\sin 2\alpha_y}{\cos^2\alpha_y \cos 2\alpha_x - \sin^2\alpha_y \cos 2\beta} \\
Y = d\dfrac{\cos(\beta-\alpha_x)\sin 2\alpha_y}{\cos^2\alpha_y \cos 2\alpha_x - \sin^2\alpha_y \cos 2\beta}
\end{cases}
. \tag{1}
$$

where d is the distance from the mirror center to the plane XOY, and α_x and α_y are the deflection angles around the X' axis and Y' axis, respectively.

The miniature objective lens group, composed of two achromatic lenses and an aspheric objective lens in the green box in Fig. 6(a), is used to simulate the real ray traces at the image plane. The simulation result is plotted in Fig. 6(d), where the blue points represent the real ray positions, which shows a barrel distortion, while the black points are calculated using the ABCD matrix of the lens group.

A Macro program based on Zemax programming language is developed for the optical model to simulate the scanning process by controlling the deflection angles α_x and α_y. The intersections (blue points) between focal spots and the imaged plane compose the real scanning pattern, as shown in Fig. 6(e). The differences between the linear and real scanning patterns result from the distortions affected by these two optical factors. The scanning pattern is rotated 180° about the X axis, and the blue points are further compressed from the XOY plane to the imaged plane due to the lens group.

B. Nonlinear Behaviors of the MEMS Mirror

In addition to the optical factors, the nonlinear movement of the MEMS mirror is another primary factor for image distortions. The scanning patterns of the MEMS mirror driven by triangular waves are measured by a position sensitive detector (PSD) (ON-Tark, PSM2-20). The experimental setup is shown in Fig. 7(a), where a collimated laser beam is reflected onto the working MEMS mirror adhered to the Part1 of the confocal probe held by a clamp, and the laser beam is then de-scanned into the PSD through a beam splitter. Fig. 7(b) displays a typical raster scanning pattern recorded by the PSD, where the slow-axis arms deflected along the y-axis at 0.05 Hz while the fast-axis
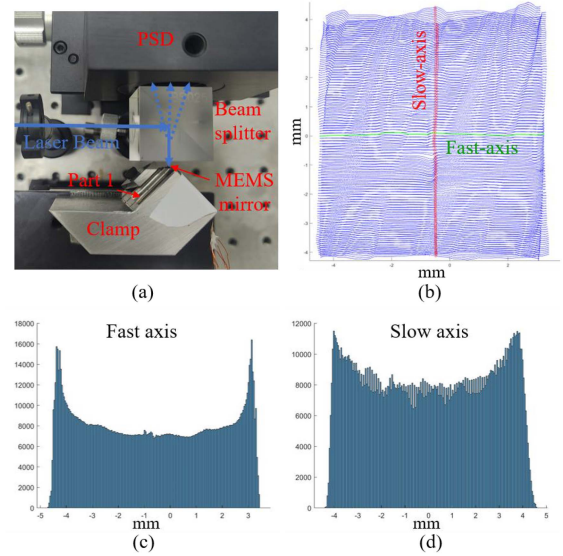

Fig. 7. The nonlinear motion test of the MEMS mirror. (a) The experimental setup for measuring the nonlinear movement. (b) A typical raster scanning pattern of the MEMS mirror actuated by triangular waves. (c) A position distribution histogram of the fast-axis scanning. (d) A position distribution histogram of the slow-axis scanning.
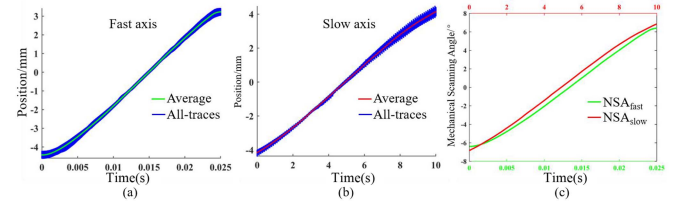

Fig. 8. The position variations of the scanning traces for fast-axis (a) and slow-axis (b) directions. (c) The mechanical scanning angle variations of the scanning traces for fast-axis and slow-axis scanning directions.

arms change the direction back and forth along the x-axis at 20 Hz. The position distributions of the raster pattern are plotted as histograms in Fig. 7(c) and (d), showing that both fast-axis and slow-axis scanning traces are not uniform. On the edges of the traces, the point density is much higher than that in the middle region, which can result in nonlinear distortions when the data are acquired using a fixed frequency.

To eliminate the influence of the nonlinear behaviors on image distortions, the characteristics of the MEMS mirror scanning movement must be figured out first. The 2D scanning traces are further analyzed to obtain the scanning angle variations of the MEMS mirror. All the fast-axis and slow-axis traces in one scanning pattern are plotted using blue lines in Fig. 8(a) and (b), respectively. The green lines and red lines are the average values of the all-traces corresponding to the fast-axis and slow-axis traces, respectively. The Euclidian distances (ED) and cosine values (CV) of all-traces are calculated to evaluate the similarity of all the traces. The average EDs are 1.23 and 1.70 for the fast and slow axis, respectively, while the average CVs are 99.96% and 99.89% for the fast and slow axis, respectively. It can be seen that the trace variations of different scanning positions
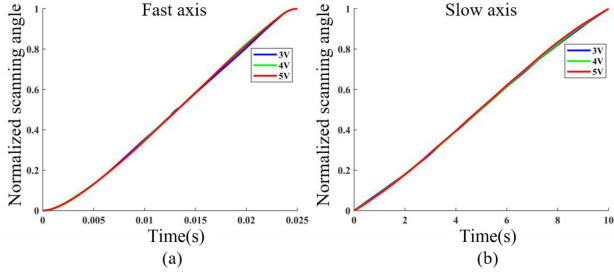
Fig. 9. The normalized curves of fast-axis (a) and slow-axis (b) mechnical scanning angles at different amplitudes of triangular waves.

have high similarity. Therefore, only two average position curves are needed to describe the nonlinear variation in each scanning pattern. The two average position curves are used to calculated the mechanical scanning angles in degree with the formula given below,

$$\theta_{x/y} = \arctan\left(\frac{L_{x/y}}{L}\right) \times \frac{180}{2\pi} \quad (2)$$

where L_x and L_y are the x-axis and y-axis positions relative to the center point, respectively, and L is the distance from the MEMS mirror to the sensing surface of the PSD. The calculated nonlinear scanning angles (NSA) for the fast and slow axis, denoted as NSA_{fast} and NSA_{slow}, respectively, are shown in Fig. 8(c).

In this MEMS-based confocal endomicroscope, the zoom function can be achieved through changing the driving voltage amplitude without the need to switch to different objectives. The reason behind the zoom control is that the FOV generated by the MEMS mirror can be regulated as shown in Fig. 1(c). Three different voltage amplitudes (3 V, 4 V and 5 V) are chosen and the corresponding scanning angle variations (normalized) of the MEMS mirror are plotted in Fig. 9(a) and (b). The average EDs are 0.078 and 0.049 for the fast and slow axis, respectively, and the average CVs are 99.99% for both axes. Therefore, the NSA variations under three driving voltage amplitudes have high similarity in both fast-axis and slow-axis scanning processes, and only one scanning pattern driven at one voltage amplitude is required to obtain the NSA variations for the distortion correction.

C. Correction Method

Once the NSA variations are known, the optical scanning model described in Fig. 6(a) can be used to obtain the real scanning pattern. A mathematical manipulation is used to describe the confocal imaging process, consisting of sampling and image reconstruction, as shown in Fig. 10. In the sampling process shown in Fig. 10(a), the intensity values $H(x_i, y_j)$ of an equally-spaced stripe object are acquired at positions $RSP(i, j)$ labeled as blue points. RSP is a M×N matrix. M and N are determined by the following equations,

$$\begin{cases} i = 1, 2, \ldots, M; M = Freq_F/2Freq_S \\ j = 1, 2, \ldots, N; N = Freq_A/2Freq_F \end{cases} \quad (3)$$
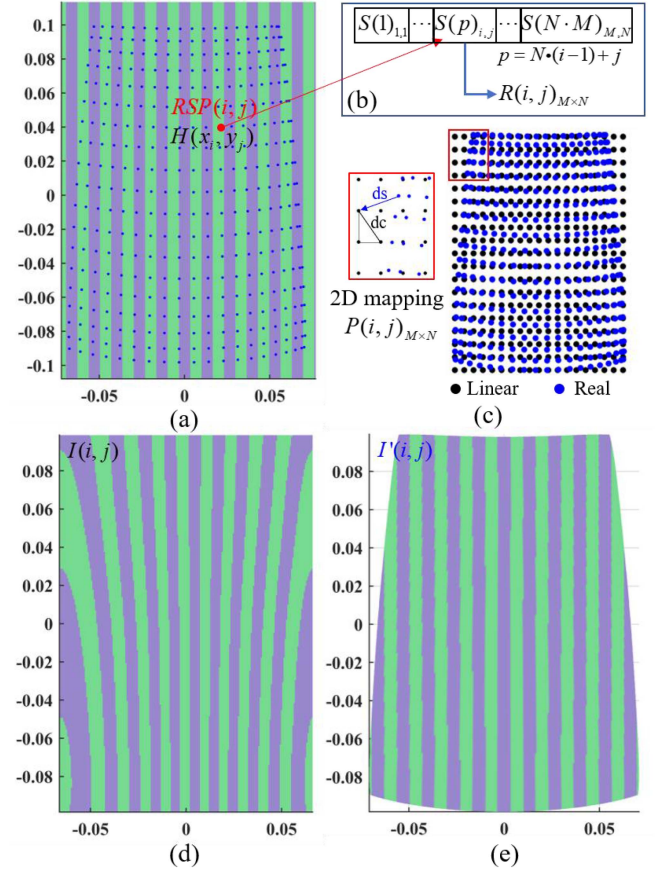

Fig. 10. Simulation of the image distortions and correction. (a) The sampled object using real scanning pattern $RSP(i, j)$. (b) 1-D raw data $S(p)_{i,j}$. (c) The 2-D mapping from 1-D raw data to 2-D image. (d) The raw image $I(i, j)$ constructed using the linear mapping. (e) The image $I'(i, j)$ corrected using real mapping.

where $Freq_F$ and $Freq_S$ are the fast and slow-axis scanning frequencies of the MEMS mirror, and $Freq_A$ is the data acquisition frequency. These intensity values of the 2D plane are sequentially stored as a 1D time serial data $S(p)_{i,j}$, which is transformed into a 2D matrix $R(i, j)_{M \times N}$, as shown in Fig. 10(b). The image reconstruction process can be treated as an inverse problem, i.e., it needs to map the raw data $R(i, j)$ to a 2D greyscale image $I(i, j)$ with the spatial mapping $P(i, j)$, where P is also a M×N matrix. As shown in Fig. 10(c), the real mapping P_{Real} is the ray-tracing results at the image plane and fuses three distortions through adding the NSAs into the optical model, where the deflection angles are given by

$$\begin{cases} \alpha_x = NSA_{slow}(i), i = 1, 2, \ldots, M \\ \alpha_y = NSA_{fast}(j), j = 1, 2, \ldots, N \end{cases} \quad (4)$$

When using the linear mapping with a uniform spatial interval, the raw image $I(i, j)$ will generate distortions, as shown in Fig. 10(d), where obvious bending and expansion of the marginal regions can be seen due to the optical and nonlinear distortions. Inversely, if the real spatial mapping is consistent with the RSP, the data S can be reconstructed as an actual image $I'(i, j)$ without any distortions, as shown in Fig. 10(e). It should be
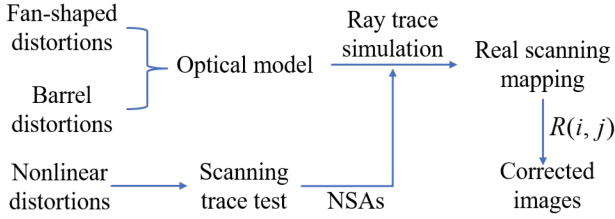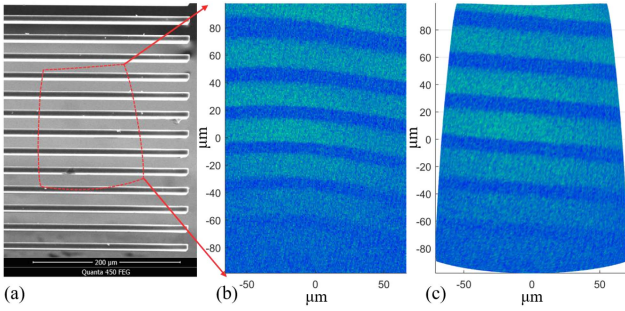
Fig. 11. The method of distortion correction.

Fig. 12. Fluorescence confocal images of a microfabrication target. (a) An SEM image of the microfabrication target with silicon cantilever beams. (b) A confocal image of the region in the dashed box in (a). (c) The corrected image of (b).
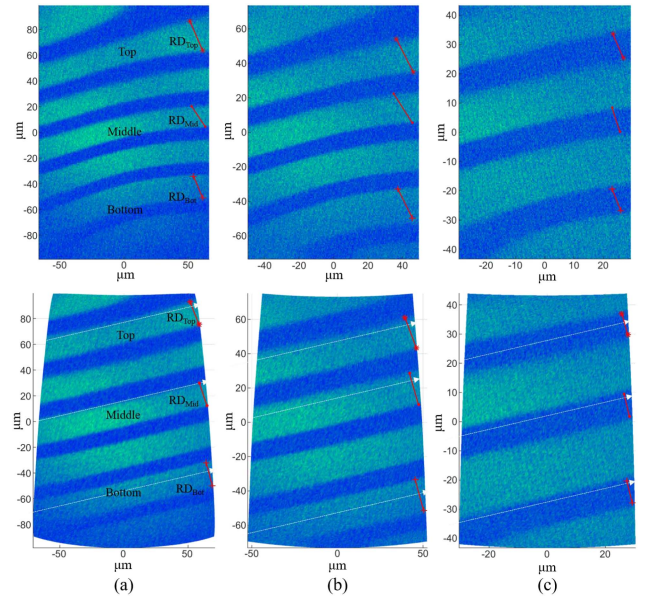

Fig. 13. The results of the distortion corrections at three driving amplitudes of 5 V (a), 4 V (b) and 3 V (c), respectively. Top row: raw confocal images. Bottom row: corrected confocal images.

noted that the stripes of the reconstructed images are not smooth because of the transformation from the point values into the pixel values.

The method of distortion correction is outlined in Fig. 11. This designed optical model inherently has the properties of the fan-shaped and barrel distortions, and the nonlinear distortions are calculated from the motion traces of the MEMS mirror. The obtained NSAs are fused in the optical model to generate the real scanning mapping using the ray-trace simulation. Therefore, three distortions are integrated in this mapping, and the real mapping is used to correct three distortions of the raw data $R(i, j)$ in one step.

IV. EXPERIMENTAL VERIFICATION

A microfabrication target with fine microstructures is used to verify the imaging performance of the confocal endoscopy system. Fig. 12(a) shows an SEM photograph of the target, which includes silicon cantilever beams that are 420 μm long and 7.7 μm wide with gaps of 18.7 μm. The target is fixed on the bottom of a glass dish before filled with an ICG solution (10 μM). The red dashed box in Fig. 12(a) is the imaging region and the corresponding raw confocal image is shown in Fig. 12(b), where the beams appear curved and the rim area is expanded. The confocal raw image is corrected using the real mapping $P(i, j)$, and the corrected image reveals that the curved beams are straightened, as shown in Fig. 12(c).

The different imaging FOVs are used to verify this method and zoom function of the CLE. The raw confocal images shown in Fig. 13(a)–(c) are scaled by using the amplitudes of the driving signals at 5 V, 4 V and 3 V. The corresponding corrected images are shown at the bottom, where NSAs of the MEMS mirror

driven at only 5 V amplitude are used in the optical model. These corrected images show that the beams are more uniform and parallel to each other compared with those raw images. Only one pair of NSAs is needed, which greatly reduces the workload of measuring the nonlinear motion characteristics of the MEMS mirror.

The confocal images obtained at different driving voltages are considered as three repeated samples for statistical analysis. Three pairs of points at the edges of the stripes on the top, middle and bottom regions are chosen to evaluate the effects of local corrections for length dimensions, as illustrated in Fig. 13. The following equations are used to quantify the degree of distortion,

$$Distortion(\%) = \left(\frac{RD - AD}{AD} \right) \times 100\%. \quad (5)$$

where the actual distances (AD) in the target are obtained using an optical microscope, and the reconstructed distance (RD) between a pair of points are represented by the red lines in the raw and corrected images. A pair of points are chosen in the corrected images according to the white auxiliary arrows assumed to be parallel to the stripes, and the straight lines connecting the two points are approximately perpendicular to the white arrows. The distortion results are represented by a bar graphs with the mean and standard deviation (SD) values, as shown in Fig. 14(a). The distortion is reduced from 21.49% to −1.40% in the top region and from 7.36% to −0.61% in the middle region. Therefore, the whole factors including the optical and micromirror factors result in an expansion especially at the border of the raw images. The negative signs here represent that the RD is less than AD. The SD values of the raw image distortions are large because of the differences between the optical distortions in three different scanning angles. Another reason is that the degree of distortion depends on the position, as shown in Fig. 14(b). The distortions
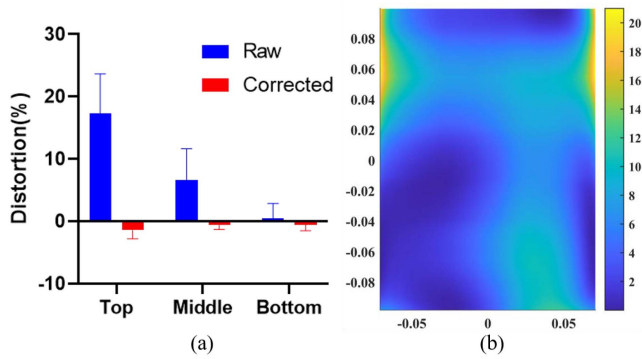
Fig. 14. (a) The results of the local distortion in the raw and corrected images. (b) The distortions between the linear and real scanning patterns.

are calculated as

$$Distortion(\%) = \left(\frac{ds - dc}{dc} \right) \times 100\% \qquad (6)$$

where ds is the offset distance from a blue point in the real mapping to the corresponding black point in the linear mapping, and dc is the hypotenuse length of the triangle composed of the adjacent points in the linear mapping, as shown in Fig. 10(c). In addition, the differences of the chosen points also affect the degree of distortion.

The image processing algorithm runs on a desktop computer with an AMD Ryzen 3 3200G CPU and 16 GB RAM and is implemented by MATLAB programming language. In our implementation, the time cost of the image correction in Fig. 13(a) is 0.26 seconds. The robustness of this method will be affected by the stability of the MEMS scanning motion, which may have a slight variation after working for long time. The information of the imaged stripes may be used to obtain the scanning traces to make the distortion correction more robust in the future. The correction results may also be influenced by the probe assembling precision, which can be improved through the precision machining technology.

V. Conclusion

In this work, a completely sealed fluorescence confocal endomicroscope is designed and constructed. This probe has simple structure and assembly process for large scale production. Most importantly, the distortions resulted from the optical layout, small lenses, and the nonlinear scanning of the MEMS mirror are corrected effectively through an optical model method. This method produces a predicted 2D mapping that can be used for distortion-free image reconstruction, and it is particularly useful in fluorescence imaging, like two-photon imaging, where a checkboard is inconvenient to use for calibration. This method has been experimentally verified using several confocal fluorescence images of a microfabrication structure. In the future, the information of the image features will be explored to calibrate the MEMS scanning traces that may be drifted after long-time use to make this method more robust. This type of miniature MEMS-based confocal probes may facilitate CLE technology to clinical extension with more systematic investigations.

References

[1] J.-A. Conchello and J. W. Lichtman, "Optical sectioning microscopy," *Nature Methods*, vol. 2, no. 12, pp. 920–931, 2005, doi: 10.1038/nmeth815.

[2] M. Goetz, N. P. Malek, and R. Kiesslich, "Microscopic imaging in endoscopy: Endomicroscopy and endocytoscopy," *Nature Rev. Gastroenterol. Hepatol.*, vol. 11, no. 1, pp. 11–18, Jan. 2014, doi: 10.1038/nrgastro.2013.134.

[3] S. Sanduleanu, A. Driessen, E. Gomez-Garcia, W. Hameeteman, A. de Bruine, and A. Masclee, "In vivo diagnosis and classification of colorectal neoplasia by chromoendoscopy-guided confocal laser endomicroscopy," *Clin. Gastroenterol. Hepatol.*, vol. 8, no. 4, pp. 371–378, Apr. 2010, doi: 10.1016/j.cgh.2009.08.006.

[4] M. J. Waldner, S. Wirtz, C. Neufert, C. Becker, and M. F. Neurath, "Confocal laser endomicroscopy and narrow-band imaging-aided endoscopy for *in vivo* imaging of colitis and colon cancer in mice," *Nature Protoc.*, vol. 6, no. 9, pp. 1471–1481, Sep. 2011, doi: 10.1038/nprot.2011.377.

[5] J. M. Jabbour, M. A. Saldua, J. N. Bixler, and K. C. Maitland, "Confocal endomicroscopy: Instrumentation and medical applications," *Ann. Biomed. Eng.*, vol. 40, no. 2, pp. 378–397, Feb. 2012, doi: 10.1007/s10439-011-0426-y.

[6] S. S. Chauhan et al., "Confocal laser endomicroscopy," *Gastrointestinal Endoscopy*, vol. 80, no. 6, pp. 928–938, Dec. 2014, doi: 10.1016/j.gie.2014.06.021.

[7] M. Rangrez, L. Bussau, K. Ifrit, and P. Delaney, "Fluorescence in vivo endomicroscopy: High-resolution, 3-dimensional confocal laser endomicroscopy (Part 1)," *Microsc. Today*, vol. 29, no. 2, pp. 32–37, 2021, doi: 10.1017/s155192952100050x.

[8] L. Yang, J. Wang, G. Tian, J. Yuan, Q. Liu, and L. Fu, "Five-lens, easy-to-implement miniature objective for a fluorescence confocal microendoscope," *Opt. Exp.*, vol. 24, no. 1, pp. 473–484, 2016, doi: 10.1364/OE.24.000473.

[9] H. Zhang and X. Ye, "The development and clinical application of microscopic endoscopy for in vivo optical biopsies: Endocytoscopy and confocal laser endomicroscopy," *Photodiagnosis Photodynamic Ther.*, vol. 38, 2022, Art. no. 102826, doi: 10.1016/j.pdpdt.2022.102826.

[10] J.-B. Kim, J. Jeon, K. Hwang, D. Y. Kim, and K.-H. Jeong, "Objective-lens-free confocal endomicroscope using Lissajous scanning lensed-fiber," *J. Opt. Microsystems*, vol. 1, no. 3, pp. 034501–034501, 2021, doi: 10.1117/1.Jom.1.3.034501.

[11] Y. H. Seo, K. Hwang, and K. H. Jeong, "1.65 mm diameter forward-viewing confocal endomicroscopic catheter using a flip-chip bonded electrothermal MEMS fiber scanner," *Opt. Exp.*, vol. 26, no. 4, pp. 4780–4785, Feb. 2018, doi: 10.1364/OE.26.004780.

[12] Z. Qiu and W. Piyawattanametha, "MEMS based fiber optical microendoscopes," *Displays*, vol. 37, pp. 41–53, 2015, doi: 10.1016/j.displa.2014.12.001.

[13] X. Duan, H. Li, F. Wang, X. Li, K. R. Oldham, and T. D. Wang, "Three-dimensional side-view endomicroscope for tracking individual cells in vivo," *Biomed. Opt. Exp.*, vol. 8, no. 12, pp. 5533–5545, Dec. 2017, doi: 10.1364/BOE.8.005533.

[14] G. Li et al., "Ultra-compact microsystems-based confocal endomicroscope," *IEEE Trans. Med. Imag.*, vol. 39, no. 7, pp. 2406–2414, Jul. 2020, doi: 10.1109/TMI.2020.2971476.

[15] I. W. Jung, D. Lopez, Z. Qiu, and W. Piyawattanametha, "2-D MEMS scanner for handheld multispectral dual-axis confocal microscopes," *J. Microelectromech. Syst.*, vol. 27, no. 4, pp. 605–612, 2018, doi: 10.1109/jmems.2018.2834549.

[16] T. Liu, M. Rajadhyaksha, and D. L. Dickensheets, "MEMS-in-the-lens architecture for a miniature high-NA laser scanning microscope," *Light: Sci. Appl.*, vol. 8, 2019, Art. no. 59, doi: 10.1038/s41377-019-0167-5.

[17] Z. Qiu et al., "Large displacement vertical translational actuator based on piezoelectric thin films," *J. Micromech. Microeng.*, vol. 20, no. 7, Jul. 2010, Art. no. 075016, doi: 10.1088/0960-1317/20/7/075016.

[18] Z. Qiu, C. H. Rhee, J. Choi, T. D. Wang, and K. R. Oldham, "Large stroke vertical PZT microactuator with high-speed rotational scanning," *J. Microelectromech. Syst.*, vol. 23, no. 2, pp. 256–258, Apr. 2014, doi: 10.1109/JMEMS.2014.2303643.

[19] C. L. Arrasmith, D. L. Dickensheets, and A. Mahadevan-Jansen, "MEMS-based handheld confocal microscope for in-vivo skin imaging," *Opt. Exp.*, vol. 18, pp. 3805–3819, 2010, doi: 10.1364/OE.18.003805.

[20] K. Jia, S. Pal, and H. Xie, "An electrothermal tip–tilt–piston micromirror based on folded dual S-shaped bimorphs," *J. Microelectromech. Syst.*, vol. 18, no. 5, pp. 1004–1015, Oct. 2009, doi: 10.1109/jmems.2009.2023838.

[21] L. Liu, E. Wang, X. Zhang, W. Liang, X. Li, and H. Xie, "MEMS-based 3D confocal scanning microendoscope using MEMS scanners for both lateral and axial scan," *Sensors Actuators A Phys.*, vol. 215, pp. 89–95, Aug. 2014, doi: 10.1016/j.sna.2013.09.035.

[22] C. L. Arrasmith and A. Mahadevan-Jansen, "MEMS-based handheld confocal microscope for in-vivo skin imaging," *Opt. Exp.*, vol. 18, no. 4, pp. 3805–3819, Feb. 2010, doi: 10.1364/OE.18.003805.

[23] R. Shintate, T. Ishii, J. Ahn, J. Y. Kim, C. Kim, and Y. Saijo, "High-speed optical resolution photoacoustic microscopy with a MEMS scanner: Novel and simple distortion correction method," *Sci. Rep.*, vol. 12, 2021, Art. no. 9221, doi: 10.21203/rs.3.rs-1044038/v1.

[24] M. Strathman et al., "MEMS scanning micromirror for optical coherence tomography," (in eng), *Biomed. Opt. Exp.*, vol. 6, no. 1, pp. 211–224, Jan. 2015, doi: 10.1364/boe.6.000211.

[25] A. Cogliati et al., "MEMS-based handheld scanning probe with pre-shaped input signals for distortion-free images in Gabor-domain optical coherence microscopy," *Opt. Exp.*, vol. 24, no. 12, pp. 13365–13374, 2016, doi: 10.1364/OE.24.013365.

[26] T. Liu, T. Pan, P. Wang, S. Qin, and H. Xie, "Scanning optimization of an electrothermally-actuated MEMS mirror for applications in optical coherence tomography endoscopy," *Sensors Actuators A: Phys.*, vol. 335, 2022, Art. no. 113377, doi: 10.1016/j.sna.2022.113377.

[27] X. Wang, Y. Xie, H. Liang, and N. Zhong, "Analysis of distortion based on 2D MEMS micromirror scanning projection system," *Micromachines (Basel)*, vol. 12, no. 7, Jul. 2021, doi: 10.3390/mi12070818.

[28] D. Wang, P. Liang, S. Samuelson, H. Jia, J. Ma, and H. Xie, "Correction of image distortions in endoscopic optical coherence tomography based on two-axis scanning MEMS mirrors," *Biomed. Opt. Exp.*, vol. 4, no. 10, pp. 2066–2077, Oct. 2013, doi: 10.1364/BOE.4.002066.

[29] H. L. Xin Miao, Y. Zhang, F. Wang, and X. Shi, "Analysis and correction of image distortion in MEMS galvanometer scanning confocal system," *Infrared Laser Eng.*, vol. 50, no. 2, 2021, Art. no. 20200206, doi: 10.3788/irla20200206.

[30] M. Hafez, T. Sidler, and R.-P. Salathe, "Study of the beam path distortion profiles generated by a two-axis tilt single-mirror laser scanner," *Opt. Eng.*, vol. 42, no. 4, pp. 1048–1057, 2003, doi: 10.1117/1.1557694.

[31] A. Jain and H. Xie, "Microendoscopic confocal imaging probe based on an LVD microlens scanner," *IEEE J. Sel. Topics Quantum Electron.*, vol. 13, no. 2, pp. 228–234, Mar./Apr. 2007, doi: 10.1109/jstqe.2007.893112.

[32] Zemax OpticStutio, Ansys, Inc., Canonsburg, PA, USA. [Online]. Available: https://www.zemax.com/

[33] M. Müller, "Confocal fluorescence microscopy," in *Introduction to Confocal Fluorescence Microscopy*, 2th ed. Bellingham, WA, USA: SPIE, 2006, ch. 1, sec. 1.3, pp. 14–21.